

Metal halide thermoelectrics: prediction of high-performance CsCu₂I₃

Jong Woong Park,¹ Young-Kwang Jung,^{2,*} and Aron Walsh^{3,4,*}

¹*Department of Materials Science and Engineering, Yonsei University, Seoul 03722, South Korea*

²*Department of Chemical Engineering and Biotechnology,
University of Cambridge, Cambridge CB3 0AS, UK*

³*Department of Materials, Imperial College London, Exhibition Road, London SW7 2AZ, UK*

⁴*Department of Physics, Ewha Womans University, Seoul 03760, South Korea*

(Dated: May 22, 2023)

Thermoelectric devices can directly convert waste heat into electricity, which makes them an important clean energy technology. The underlying materials performance can be evaluated by the dimensionless figure of merit ZT . Metal halides are attractive candidates due to their chemical flexibility and ease of processing; however, the maximum ZT realized ($ZT = 0.15$) falls far below the level needed for commercialization ($ZT > 1$). Using a first-principles procedure we assess the thermoelectric potential of copper halide CsCu₂I₃, which features 1D Cu–I connectivity. The n-type crystal is predicted to exhibit a maximum ZT of 2.2 at 600 K along the b -axis. The strong phonon anharmonicity of this system is shown by locally stable non-centrosymmetric $Amm2$ structures that are averaged to form the observed centrosymmetric $Cmcm$ space group. Our work provides insights into the structure–property relations in metal halide thermoelectrics and suggests a path forward to engineer higher-performance heat-to-electricity conversion.

I. INTRODUCTION

Thermoelectric materials – which enable the direct conversion of waste heat to electricity – have received great attention as one of the most promising renewable energy technologies [1]. The performance of thermoelectric materials is evaluated by the dimensionless figure of merit, ZT :

$$ZT = \frac{S^2 \sigma T}{\kappa_{\text{elec}} + \kappa_{\text{latt}}} \quad (1)$$

where S is the Seebeck coefficient, σ is the electrical conductivity, T is the temperature, κ_{elec} is the electronic thermal conductivity, and κ_{latt} is the lattice thermal conductivity (power factor, PF , is defined as $S^2 \sigma$). Due to the recent progress in calculation methods for electron (hole) and phonon transport in solid crystals, computational studies have been made to discover novel compounds that possess a high ZT [2–5]. Although the trade-off effect between the parameters that control ZT makes the optimization challenging, search for an intrinsically low κ_{latt} material is still crucial to maximize performance [6]. In other words, high thermoelectric performance requires the phonons to be disrupted like in a glass but the electrons to have a high mobility like in crystalline semiconductors (i.e. phonon-glass electron-crystal) [7].

A. Metal halide thermoelectrics

Metal halides have been studied for their uses in various applications including solar cells [8, 9], light-emitting

diodes [10, 11], and memristors [12, 13]. These materials are also known to have an intrinsically ‘ultra-low’ κ_{latt} ($< 1 \text{ W/m}\cdot\text{K}$) [14–16], and several reports have started to suggest their potential for thermoelectric applications (Table I).

However, the highest maximum ZT of 0.15 achieved from a halide perovskite CsSnI₃ [18] is far to compete with top thermoelectric materials such as SnSe whose maximum ZT is > 2.6 [29]. In addition, studies were mainly conducted on conventional halide perovskites, while emerging low-dimensional metal halides have yet to be explored. Recently, we reported a high thermoelectric potential in metal halide Cs₃Cu₂I₅ for the first time where asymmetric heat and charge transport in the material enables a high maximum ZT of 2.6 at 600 K [28].

In this article, we present CsCu₂I₃ as a candidate for thermoelectric applications on the basis of first-principles predictions. CsCu₂I₃ is one of the copper-based low-dimensional halide compounds where 1D [Cu₂I₃][−] anionic chains are separated by Cs⁺ cations. By performing lattice dynamics simulations, we found that heat transport in the material is highly anisotropic where the κ_{latt} in the ab -plane (perpendicular to the chains) is about 2 times lower than that along the c -axis (chain direction). We also confirmed that the experimentally reported $Cmcm$ structure of the material is not dynamically stable but an average of $Amm2$ structures during our phonon analysis. Interestingly, electron transport in the material shows an opposite anisotropy compared to the phonon transport; electron mobility in the ab -plane is 1.5 times higher than that along the c -axis. Due to this unique anisotropy of heat and electron transport in a single material, we predict that the CsCu₂I₃ in $Amm2$ structure reaches a ZT of 2.2 at 600 K along the b -axis, having potential as a next-generation thermoelectric material.

* yj359@cam.ac.uk; a.walsh@imperial.ac.uk

TABLE I. Representative works on metal halides studies for thermoelectric devices with their κ_{latt} and ZT values. The mentioned values are for room temperature unless indicated otherwise.

	Compound	κ_{latt} (W/m·K)	ZT	κ measurement	Ref.
Conventional perovskites	CsSnI ₃	0.38	0.11 (320 K)	NW thermometry	[15]
	CsSnI ₃	0.28	0.08 (323 K)	3- ω method	[17]
	CsSnI ₃	0.60	0.15 (550 K)	Laser flash method	[18]
	CsSnI ₃ + SnCl ₂ 1%	0.38	0.14 (345 K)	3- ω method	[19]
	CsSnI ₃ + PbI ₂ 0.5%		0.14 (523 K)	Laser flash method	[20]
	CsSn _{0.8} Ge _{0.2} I ₃		0.12 (473 K)	Laser flash method	[21]
	CsSnBr ₃	0.64		Laser flash method	[18]
	CsPbI ₃	0.45		NW thermometry	[15]
	CsPbBr ₃	0.42		NW thermometry	[15]
	CsPbBr ₃	0.44 (tot.)		3- ω method	[22]
	CsPbBr ₃	0.46 (tot.)		FDTR	[23]
	CsPbCl ₃	0.49 (tot.)		3- ω method	[24]
	Cs ₂ SnI ₆	0.29		Laser flash method	[25]
	Low-D metal halides	Cs ₂ SnI ₂ Cl ₂	0.60 (300 K)		Laser flash method
CsPb ₂ Br ₅		0.32 (tot.)		3- ω method	[22]
Cs ₂ PbI ₂ Cl ₂		0.45 (300 K)		Laser flash method	[26]
Cs ₂ PbI ₂ Cl ₂		0.37 (295 K)		Laser flash method	[27]
Cs ₄ PbCl ₆		0.30 (tot.)		3- ω method	[24]
Cs ₃ Cu ₂ I ₅		0.02	2.6 (600 K)	Phono3py (theory)	[28]
CsCu ₂ I ₃		0.05 (300 K)	0.4 (300 K)	Phono3py (theory)	This study
		0.02 (600 K, <i>b</i> -axis)	2.2 (600 K, <i>b</i> -axis)		

II. RESULTS AND DISCUSSION

A. First-principles thermoelectrics workflow

The workflow to predict ZT from first principles is shown in Fig. 1. In principle, this only requires prior knowledge of a crystal structure and all other properties can be directly calculated in turn. As the first step, the crystal structure of a compound of interest should be optimized to a local minimum in the potential energy surface. If the compound shows imaginary phonon modes, additional crystal structure optimization and/or anharmonic corrections should be applied to obtain dynamically stable structure, so that reliable thermal properties can be calculated [30]. With the dynamically stable crystal structure, bulk properties can be assessed. Results from steps 2–4 are given as inputs for calculating carrier lifetimes and transport properties – S , σ , and κ_{elec} (step 5), while lattice thermal conductivity, κ_{latt} is obtained from anharmonic phonon calculations (steps 6 and 7). Finally, thermoelectric properties such as ZT and thermodynamic efficiency (η) are predicted by combining the outputs from steps 5 and 7. Computational details are provided in section IV.

B. Structural analysis

CsCu₂I₃ has been reported in a $Cmcm$ space group, [31, 32] where 1D [Cu₂I₃][−] anionic chains are separated by Cs⁺ cations as shown in Fig. 2. When the experimentally known structure was adopted and optimized, we

found that imaginary phonon modes are persistent across the first Brillouin zone (see Fig. 3(a)), which confirms dynamic structural instability of the $Cmcm$ structure. (This will be further discussed in section II C). To obtain a dynamically stable crystal structure, we deformed the $Cmcm$ structure along the eigenvector of its imaginary Γ phonon mode, which results in a structural transition to new lower-symmetry $Amm2$ phase. The structural transition from $Cmcm$ to $Amm2$ occurs with atomic positions shifted along the directions indicated by the arrows in Fig. 2(a), (c). Cs and I atoms move within the b -axis and ab -plane, respectively, while Cu atoms move along the c -axis. The Cu–I–Cu bond angle for $Cmcm$ is alternately 71.54° and 71.16°, while polyhedra distortion in $Amm2$ results in a bond angle of 61.39° and 81.42°, as shown in Fig. 2(e). In $Cmcm$, the Cu–I bond lengths in the [CuI₄]^{3−} tetrahedron are of a similar value (2.62 and 2.61 Å, two each), as opposed to the bonds in $Amm2$ all having a different value (2.66, 2.65, 2.58, and 2.61 Å). Thus, while the crystal system is maintained as orthorhombic, the crystal symmetry is lowered from centrosymmetric $Cmcm$ to non-centrosymmetric $Amm2$. Comparison of the calculated lattice parameters of $Cmcm$ and $Amm2$, as well as experimental value from X-ray diffraction measurement are provided in Table II. The structural transition results in a_0 decreasing 0.30% while b_0 increasing 0.84%, both changes due to the movement of Cs and I atoms. In contrast, c_0 is equivalent in both structures, as the shift of Cu atoms even out macroscopically. $Amm2$ has an expanded volume of 0.70% compared to $Cmcm$. The elastic and dielectric tensors calculated from $Cmcm$ and $Amm2$ phases are provided in Table S1.

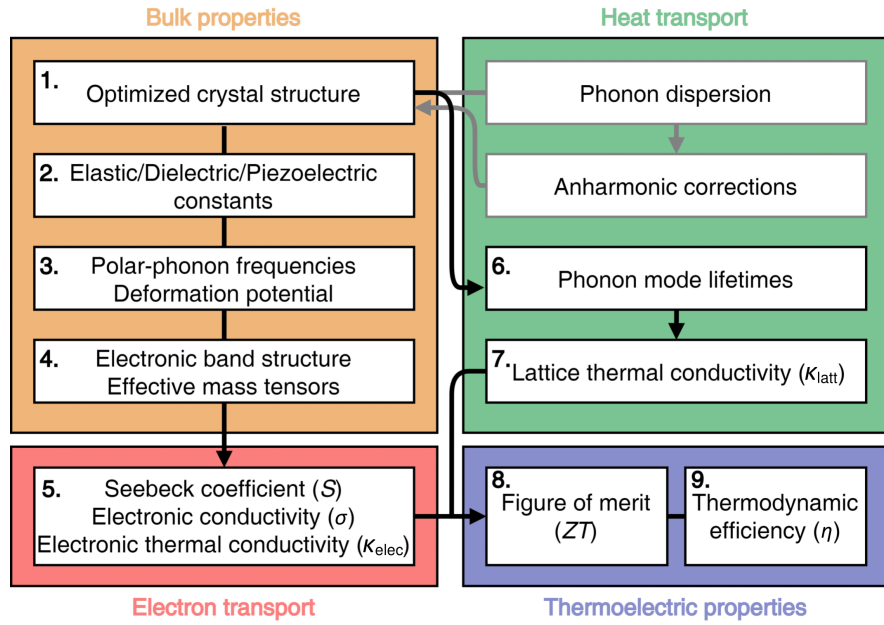


FIG. 1. Diagram for a first-principles thermoelectrics assessment workflow (total 9 steps). Steps which are optional or only required in certain cases are shown by gray boxes and arrows.

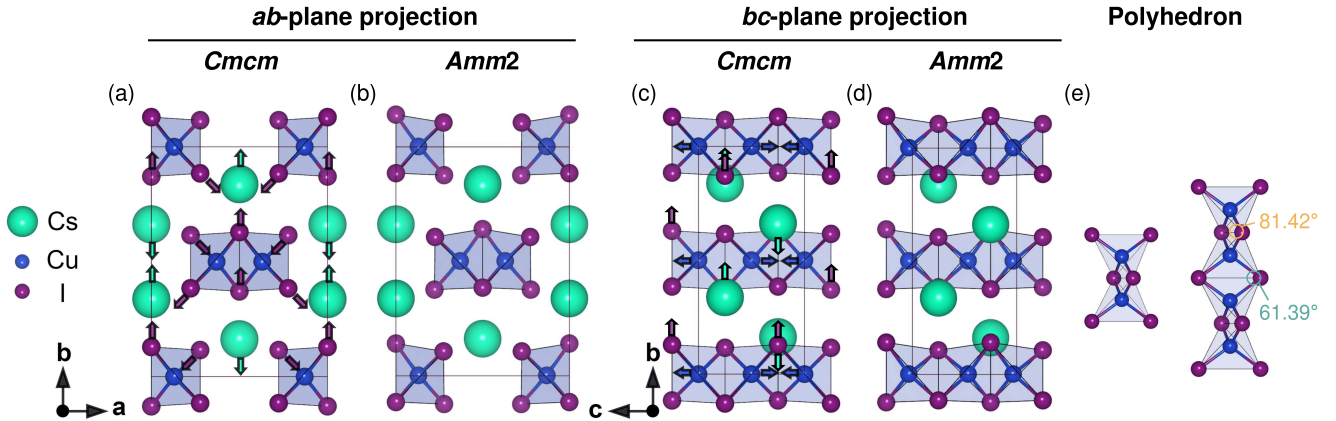


FIG. 2. Projected crystal structure of CsCu_2I_3 (a) $Cmcm$ and (b) $Amm2$ to the ab -plane, and to the bc -plane of (c) $Cmcm$ and (d) $Amm2$. Arrows indicate the directions which the atoms move when the $Cmcm$ to $Amm2$ transition occurs. (e) Polyhedron of $Amm2$ (left) and its linked structure (right). Cu-I-Cu bond angles are indicated.

TABLE II. Calculated lattice parameters (a_0 , b_0 , c_0) and volume (V_0) of the conventional orthorhombic unit cell for both polymorphs of CsCu_2I_3 , and experimental value from X-ray diffraction measurement.

	a_0 (\AA)	b_0 (\AA)	c_0 (\AA)	V_0 (\AA^3)
$Cmcm$	10.06	13.08	6.10	802.3
$Amm2$	10.03	13.19	6.10	807.9
Exp. [33]	10.55	13.17	6.10	847.4

C. Dynamic structural instability

The phonon dispersion of $Cmcm$ and $Amm2$ is illustrated together with the atom-projected phonon density of states (PDOS) in Fig. 3(a), (b), respectively. While the Materials Project [34] repository, as well as computational[35] and experimental[33] reports, indicate CsCu_2I_3 as a $Cmcm$ structure, dynamic structural instability of $Cmcm$ is evident by the numerous imaginary modes shown in Fig. 3(a). The eigenvector components for the imaginary mode at the Γ -point of $Cmcm$ are shown by arrows in Fig. 2(a), (c). Using

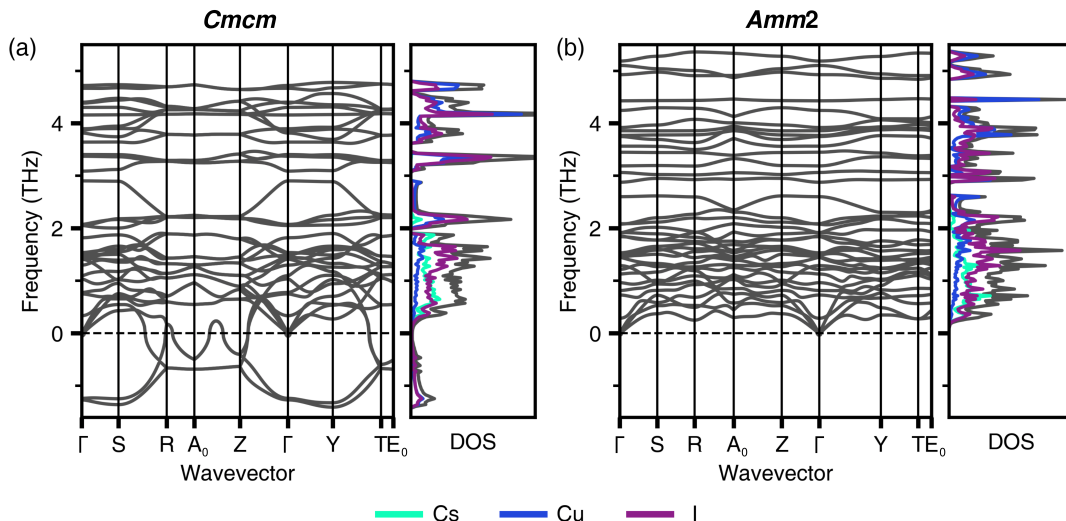


FIG. 3. Phonon dispersion of CsCu₂I₃, (a) *Cmc* and (b) *Amm2* structure. The atom-projected phonon density of states is plotted on the right side of the phonon dispersion.

MODEMAP[36], the corresponding energy as a function of the distortion amplitude along the eigenvectors illustrated in Fig. 2(a), (c) is shown in Fig. 4. A characteristic double-well potential-energy curve is shown. The saddle point corresponds to the *Cmc* structure, while the two wells indicate the lower symmetry *Amm2* structure as a local minimum. Thus, the energy-lowering distortion causes a structural transition to a ground-state polymorph, *Amm2*, with an energy 2.84 meV/atom lower than *Cmc*. As shown in Fig. 3(b), the absence of imaginary phonon modes indicates the dynamic stability of *Amm2*. Hence, we propose that the previously reported centrosymmetric *Cmc* structure is a macroscopic average over locally non-centrosymmetric *Amm2* structures. In addition, in the *Amm2* structure, a lack of inversion symmetry causes a spontaneous electric polarization. As shown in Fig. 2(a), (c), polarization mainly occurs within the *ab*-plane by the shift of Cs and I atoms, while minute polarization along the *c*-axis corresponds to the movement of Cu atoms. The corresponding piezoelectric tensor of the *Amm2* structure is provided in Table S1.

D. Ultra-low lattice thermal conductivity

Fig. 5 shows the κ_{latt} of *Amm2* CsCu₂I₃, as a function of temperature along different crystallographic directions. Because CsCu₂I₃ is experimentally reported to have a melting point at ~ 644 K [33, 37], the temperature range for calculating κ_{latt} as well as transport and thermoelectric properties discussed later is set up to 600 K. *Amm2* shows an unexpectedly low κ_{latt} (i.e. ultra-low κ_{latt}) of a value under 0.1 W/m·K for all directions even at 300 K; 0.05, 0.03, and 0.08 W/m·K for the *a*-, *b*-, and *c*-axes, respectively. The isotropically averaged κ_{latt}

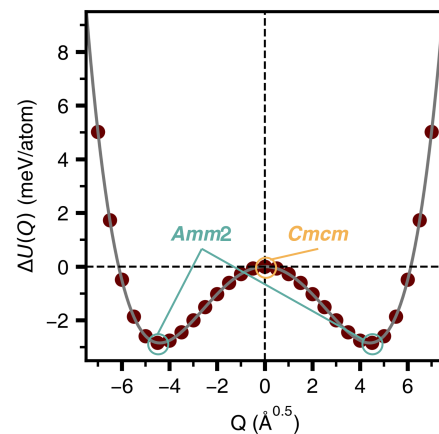


FIG. 4. Potential energy surface along the eigenvector components (arrows in Fig. 2(a), (c)) for the imaginary mode at the Γ -point of CsCu₂I₃, *Cmc* structure. Filled circles represent calculated data points, and the solid line is a fit to a polynomial function.

(κ_{avg}) at 300 K is 0.05 W/m·K, which is lower than one of the top thermoelectric materials, SnSe (0.2 W/m·K at 300 K [38]). The value is slightly higher compared to Cs₃Cu₂I₅ ($\kappa_{\text{avg}} = 0.02$ W/m·K at room temperature (RT) [28]), which was calculated at a similar level of theory. At 600 K, the κ_{latt} values are 0.02 W/m·K along the *a*- and *b*-axes, and 0.04 W/m·K along the *c*-axis (κ_{avg} being 0.03 W/m·K). The anisotropy of CsCu₂I₃, having a higher κ_{latt} along the *c*-axis, can be ascribed to a weaker chemical bonding towards the *c*-axis of the unit cell [39]. It is noteworthy that the *c*-axis is parallel to the [Cu₂I₃]⁻ chains.

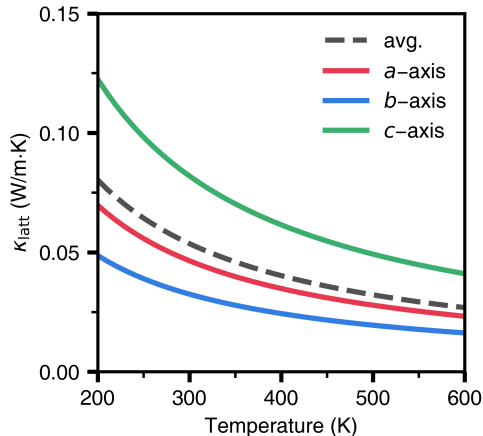


FIG. 5. Lattice thermal conductivity (κ_{latt}) of CsCu_2I_3 , $Amm2$ structure, as a function of temperature along different crystallographic axes. ‘avg.’ refers to the isotropically averaged κ_{latt} (κ_{avg}) along the three (a -, b -, and c -) axes.

Acoustic phonon modes and low-frequency optic modes act as the primary heat carriers in crystals, mainly contributing to κ_{latt} . As shown in Fig. 3(b), the low-lying optic modes of $Amm2$ are relatively flat, which leads to low group velocities (v_λ), one of the reasons for its ultra-low κ_{latt} . In addition, the high density of the low-lying optic modes produces a large number of scattering channels at this frequency range, causing short phonon lifetimes (τ_λ). Fig. S1 shows avoided crossings of the acoustic and low-frequency optic modes at the Γ -Y direction. Avoided crossing is a characteristic feature shown when a ‘rattler’ is present in the material [40]. PDOS shown in Fig. 3(b) indicates that lower-frequency phonon modes mostly comprise motions of Cs atoms. Thus, we can infer that Cs atoms behave as the rattler, rattling within the space between $[\text{Cu}_2\text{I}_3]^-$ chains. Fig. S2 shows the Cs-I bonds (total 10), and the broad range of bond lengths being from 3.81 to 4.21 Å contributes to the anharmonicity of CsCu_2I_3 . This is similar to the origin of anharmonicity of SnSe [41]. We note that fluctuations between $Cmcm$ and $Amm2$ could also contribute to the scattering of the heat transport, but such higher-order anharmonicity is not considered here.

To further understand the origins of the ultra-low κ_{latt} of CsCu_2I_3 , we analyzed the modal contributions to the net transport (Fig. 6). The net transport, κ_{latt} , is a sum of the individual phonon modes (λ):

$$\kappa_{\text{latt}} = \frac{1}{NV_0} \sum_{\lambda} \kappa_{\lambda} = \frac{1}{NV_0} \sum_{\lambda} C_{\lambda} v_{\lambda} \otimes v_{\lambda} \tau_{\lambda} \quad (2)$$

where N is the number of unit cells in the crystal (equivalent to the number of wavevectors included in the Brillouin zone summation), V_0 is the volume of the crystallographic unit cell, and C_{λ} is the modal heat capacity. The frequency spectra of v_{λ} , τ_{λ} , and phonon mean free path ($\Lambda_{\lambda} = v_{\lambda} \times \tau_{\lambda}$) at 300 K is shown in Fig. 6(a)–(c), respec-

tively [42]. In the entire frequency range, the majority of v_{λ} fall within the range between 1 and 10^3 m/s, and the fastest modes are seen at the 0–0.2 THz frequency range. The fastest modes correspond to the acoustic phonon bands that are relatively dispersive compared to the optic modes. The overall spectra is comparable to $(\text{CH}_3\text{NH}_3)\text{PbI}_3$ (MAPbI_3) [43], a 3D perovskite reported to have a ultra-low κ_{latt} of 0.05 W/m·K at 300 K, while the fastest modes have a lower v_{λ} in CsCu_2I_3 . In addition, a number of modes have a very low v_{λ} , from 10^{-12} to 10^{-10} m/s, unseen in the v_{λ} spectra of MAPbI_3 [43] and $\text{Cs}_3\text{Cu}_2\text{I}_5$ [28]. These modes correspond to the low-lying optic modes at the 0.2–2.4 THz frequency range that are relatively flat. The low v_{λ} attribute to the heavy elements that constitute CsCu_2I_3 .

τ_{λ} mostly falls into the range of 10^{-1} to 10^1 ps, while a number of phonon modes within the 0–0.2 THz frequency range (acoustic phonon modes) have a τ_{λ} longer than 10 ps. The overall spectra is similar to MAPbI_3 [43] and $\text{Cs}_3\text{Cu}_2\text{I}_5$ [28], while the longest τ_{λ} of CsCu_2I_3 are longer compared to $\text{Cs}_3\text{Cu}_2\text{I}_5$ (longest being 11 ps). The combination of a low v_{λ} and τ_{λ} leads to the majority of the modes having Λ_{λ} shorter than 10^0 nm, which is why CsCu_2I_3 shows an ultra-low κ_{latt} . The low-frequency modes (acoustic and low-lying optic modes) have a relatively faster v_{λ} and longer τ_{λ} resulting in a longer Λ_{λ} compared to the high-frequency modes. This matches with the fact that acoustic and low-lying optic modes are the primary heat carriers.

E. Electronic structure and transport properties

The electronic band structure of $Cmcm$ and $Amm2$ is illustrated in Fig. 7(a) and (b), respectively. Both $Cmcm$ and $Amm2$ phases have a direct band gap (E_g) at the Γ -point, with a E_g value of 3.23 eV and 3.08 eV, respectively. The calculated E_g is similar to the experimental value estimated from the optical absorption spectrum, 3.49 eV [37]. As shown in Fig. S3, upper valence bands are dominated by Cu 3d and I 5p orbitals, while lower conduction bands arise from the hybridization of Cu 4s and I 5p orbitals. For the conduction band minimum, I 5s contributes more compared to I 5p. Calculation of the orbitals that comprise band edges are in good agreement with previous reports [33, 37]. The contribution of Cs orbitals on those band edges is negligible, which is the well-known feature of low dimensional metal halides [44, 45]. The corresponding orbitals are also equivalent to the electronic band structure of $\text{Cs}_3\text{Cu}_2\text{I}_5$ [28]. The upper valence band is relatively flat, having a hole effective mass of $0.83 m_e$ at the valence band maximum, while the lower conduction band is relatively dispersive with an electron effective mass of $0.31 m_e$ at the conduction band minimum. Conduction band has multiple valleys (Γ -point, Z-point, and along the S–R and Y–T direction), and the energy difference between the first and second conduction band edge is 0.57 eV for $Amm2$. The dispersive nature

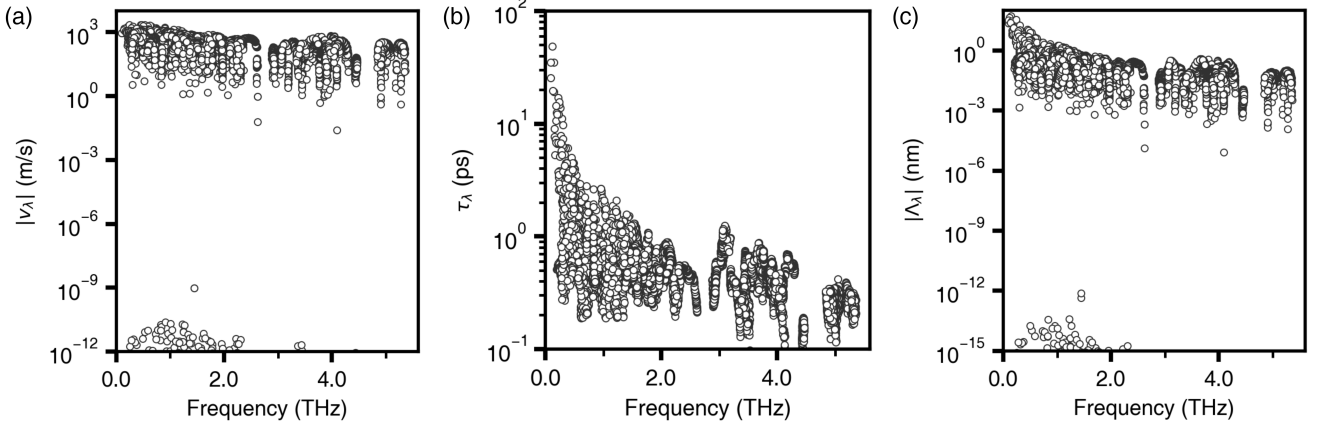


FIG. 6. Modal properties of the lattice thermal conductivity (κ_{latt}) of CsCu_2I_3 , *Amm2* structure, at 300 K; (a) group velocity norms (v_λ); (b) lifetimes (τ_λ); and (c) mean free paths ($\Lambda_\lambda = v_\lambda \times \tau_\lambda$).

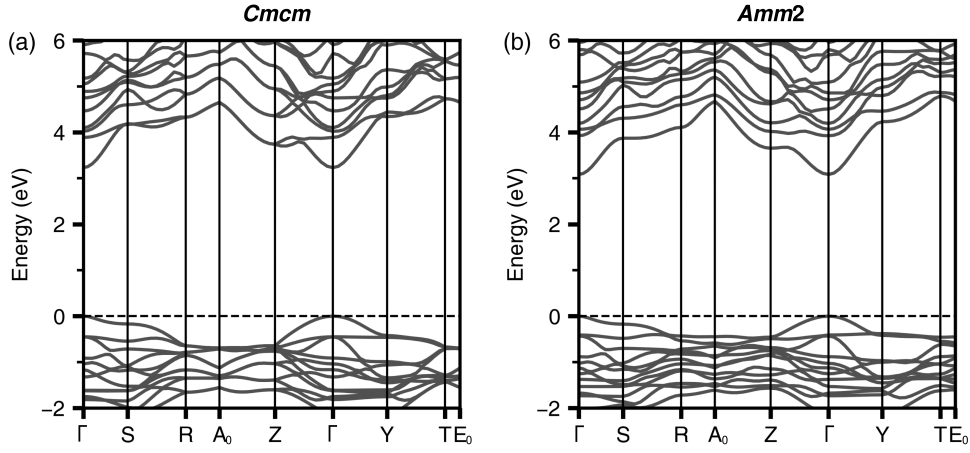


FIG. 7. Electronic band structure of CsCu_2I_3 , (a) *Cmc* and (b) *Amm2* structure (the valence band maximum is set to 0 eV).

and multiple valleys lead to a high σ and S , respectively, suggesting the possibility of CsCu_2I_3 as a promising n-type thermoelectric material.

Fig.8 shows the calculated electron mobility, μ , of *Amm2* as a function of temperature along different crystallographic directions at the optimal electron concentration, n_e , ($6 \times 10^{18} \text{ cm}^{-3}$) at which thermoelectric properties are maximized (n_e will be further discussed in Fig.10(a)). Similar to κ_{latt} , μ is anisotropic, with μ being lower along the *c*-axis. The isotropically averaged μ is $21.4 \text{ cm}^2/\text{V}\cdot\text{s}$ at 300 K, which is slightly higher than the μ of $\text{Cs}_3\text{Cu}_2\text{I}_5$ [28] ($18.2 \text{ cm}^2/\text{V}\cdot\text{s}$ at RT). Fig.S4 shows μ of *Cmc* and *Amm2* by the individual scattering mechanisms. Acoustic deformation potential (ADP), ionized impurity (IMP), and polar optical phonon (POP) scattering mechanisms were considered for both structures, and for *Amm2* (non-centrosymmetric), piezoelectric (PIE) scattering mechanism was considered as well.

μ is limited by POP scattering for both structures, followed by IMP and ADP scattering. POP scattering is dominant in many of the top thermoelectric materials including SnSe [46] and $\text{Cs}_3\text{Cu}_2\text{I}_5$ [28]. In *Amm2*, PIE scattering has the smallest contribution to the total μ , as its polarization is minute.

The electronic transport properties – σ , S , PF , and κ_{elec} – of *Amm2* as a function of temperature and n_e are shown in Fig.S5. σ and κ_{elec} are proportional to n_e , but have an inverse relationship with temperature. On the other hand, $|S|$ is disproportionate with n_e , and increases with temperature. Fig.9 shows σ , S , PF , and κ_{elec} as a function of temperature along different crystallographic directions ($n_e = 6 \times 10^{18} \text{ cm}^{-3}$). σ , κ_{elec} , and PF is higher along the *a*- and *b*-axes, which reflects the anisotropy of μ . $|S|$ is almost equivalent along all axes. Along the *b*-axis, the PF goes up to $109.66 \mu\text{W}/\text{m}\cdot\text{K}^2$ at 470 K.

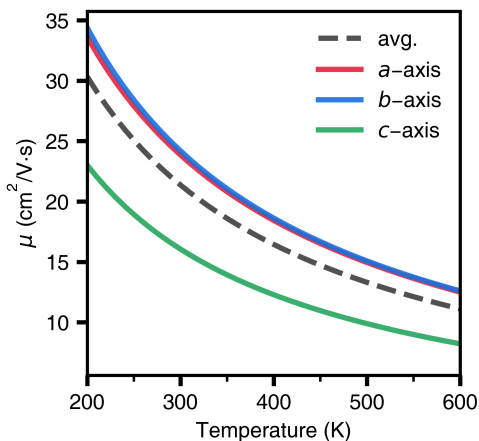


FIG. 8. Mobility (μ) of CsCu_2I_3 , $Amm2$ structure, as a function of temperature along different crystallographic axes. ‘avg.’ refers to the isotropically averaged μ along the three (a-, b-, and c-) axes (electron concentration = $6 \times 10^{18} \text{ cm}^{-3}$).

F. Thermoelectric properties

By combining the phonon and electron transport properties using Eq. (1), ZT for CsCu_2I_3 as a function of temperature along different crystallographic axes is predicted (Fig. 9(e)). Due to the anisotropy of σ , κ_{latt} , and κ_{elec} , ZT is also anisotropic, showing a lower value along the c -axis. At 600 K, it reaches a value of 2.2 along the b -axis, while the a - and c -axes has a ZT of 1.7 and 0.8, respectively. Notably, a high ZT is obtained at a lower temperature compared to the state-of-the-art thermoelectric material, n-type SnSe , which has a ZT of 2.0 above 700 K [47]. The origin of a high ZT is a combination of ultra-low κ_{latt} and high PF . Fig. 10(a) shows the isotropically averaged ZT of CsCu_2I_3 as a function of temperature and n_e . ZT is maximized at n_e of $6 \times 10^{18} \text{ cm}^{-3}$, and the maximum ZT achievable at this condition is 1.5 at 600 K. As mentioned above, the highest ZT from a conventional halide perovskite was only 0.15, so this work may derive more attention towards CsCu_2I_3 and other low-dimensional metal halides.

Thermodynamic efficiency, η , of thermoelectric generators can be calculated by the following equation:

$$\eta = \frac{T_H - T_C}{T_H} \frac{\sqrt{1 + \overline{ZT}} - 1}{\sqrt{1 + \overline{ZT}} + \frac{T_C}{T_H}} \quad (3)$$

where T_H and T_C are the hot side and cold side temperature of the generator, respectively. The average ZT (\overline{ZT}) is defined as follows:

$$\overline{ZT} = \frac{1}{(T_H - T_C)} \int_{T_C}^{T_H} ZT dT \quad (4)$$

Using these equations, we plotted η as a function of T_H , while T_C is fixed to 200 K (Fig. 10(b)). Maximum η of

13.1% is achieved when the temperature difference is 400 K ($T_H = 400 \text{ K}$), and \overline{ZT} being 0.8.

The main concern when fabricating CsCu_2I_3 for thermoelectric applications would be whether the optimal n_e could be achieved by doping. Currently, doping of perovskite derivatives is underexplored, but below we address some of the doping strategies that can be implemented. Similar to the doping approaches of 3D perovskites, doping in perovskite derivatives could be achieved either by (1) adding dopant sources to the precursor solution; (2) post-synthesis solution doping; and (3) post-synthesis vapor doping [48]. The specific methods could be adding atomic dopants, and molecular dopants by surface doping. In general, the B-site metals (Cu for CsCu_2I_3) mainly contribute to the edge of the band structure [48] (c.f. Fig. S3). Thus, substituting Cu^+ with +2 charged ions is more likely to produce the necessary states to tune n_e , compared to the doping of Cs and I.

ZT of CsCu_2I_3 is relatively low compared to $\text{Cs}_3\text{Cu}_2\text{I}_5$. However, it is reported that CsCu_2I_3 is more stable than $\text{Cs}_3\text{Cu}_2\text{I}_5$ when dopants are added, and the unstable $\text{Cs}_3\text{Cu}_2\text{I}_5$ decompose and form into CsCu_2I_3 [49]. Thus, although a higher optimal n_e is required for CsCu_2I_3 ($6 \times 10^{18} \text{ cm}^{-3}$, compared to $4 \times 10^{18} \text{ cm}^{-3}$ for $\text{Cs}_3\text{Cu}_2\text{I}_5$), it may be achieved more easily. In addition, whether this high thermoelectric performance is shown only for CsCu_2I_3 and $\text{Cs}_3\text{Cu}_2\text{I}_5$, or from perovskite derivatives in general requires further investigation. Through our initial calculations, copper-based metal halides K_2CuX_3 and CsCu_2X_3 ($X = \text{Cl}, \text{Br}$) are also expected to have a high potential as an n-type thermoelectric material. Changing the A-site or X-site elements to the ones in the same group of the periodic table is also worth a try. Thus, investigating $\text{Cs}_3\text{Cu}_2\text{X}_5$ and Rb_2CuX_3 ($X = \text{Cl}, \text{Br}$) as well as RbCu_2Y_3 ($Y = \text{Br}, \text{I}$) could be possible.

III. CONCLUSIONS

In this paper, we report a new direction for metal halide thermoelectrics with a predictive study on the structure, properties, and performance of CsCu_2I_3 .

The dynamic structural instability of the previously known $Cmcm$ structure of CsCu_2I_3 was investigated. We report a new, ground-state $Amm2$ structure of CsCu_2I_3 , and compared its basic bulk properties with $Cmcm$. The ultra-low κ_{latt} of $Amm2$ and its origins were studied in detail. Additionally, the electronic transport properties as well as ZT were first reported in this work. We predict that CsCu_2I_3 is a new promising n-type thermoelectric material, and require further investigations in low-dimensional metal halides.

The centrosymmetric $Cmcm$ structure is a macroscopic average over locally non-centrosymmetric $Amm2$ structures. The octahedra distortion leads to an energy-lowering structural transition from $Cmcm$ to $Amm2$, and the energy being 2.84 meV/atom lower. The lack of in-

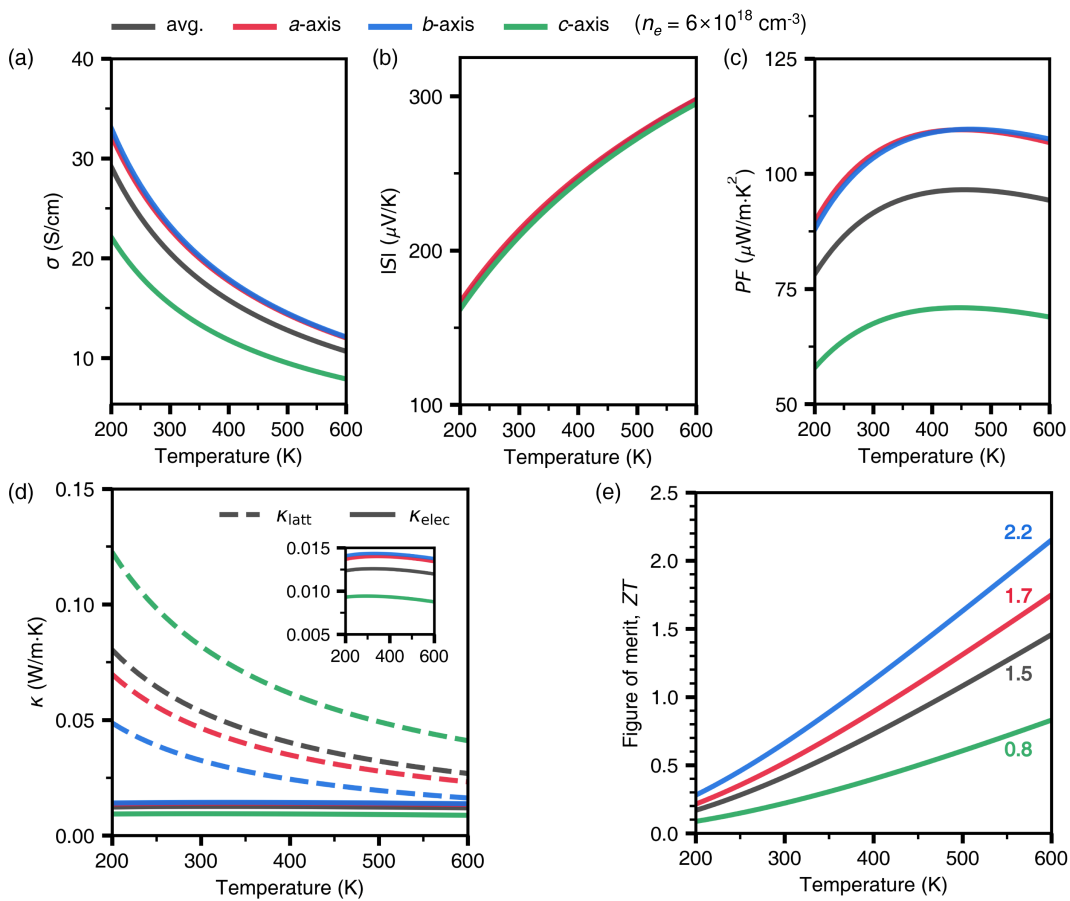


FIG. 9. Transport and thermoelectric properties of CsCu_2I_3 *Amm2* structure, as a function of temperature along different crystallographic axes. (a) Electrical conductivity (σ); (b) Seebeck coefficient (S); (c) power factor ($PF = S^2\sigma$); (d) electronic (κ_{elec} , dashed lines) and lattice (κ_{latt} , solid lines) thermal conductivity (inset figure is a zoomed plot of κ_{elec}); and (e) figure of merit (ZT) (electron concentration = $6 \times 10^{18} \text{ cm}^{-3}$).

version symmetry in *Amm2* results in a spontaneous lattice polarization mainly within the *ab*-plane.

Amm2 shows an ultra-low κ_{latt} with κ_{avg} at 300 K being 0.05 W/m·K, and the values being higher along the *c*-axis (i.e. anisotropic). The low v_λ is due to the low-frequency optic modes being relatively flat. Avoided crossings of the acoustic and low-lying optic modes are shown from the dispersion, which is the cause of short τ_λ . Cs atoms between the $[\text{Cu}_2\text{I}_3]^-$ chains behave as rattlers, and the inequivalent Cs-I bond lengths give rise to a strong anharmonicity. The structural transition between *Cmcm* and *Amm2* could also contribute to the phonon scattering.

The conduction bands of CsCu_2I_3 is relatively dispersive and has multiple valleys, which is the reason for its high σ and S , respectively, characteristics of a novel n-type thermoelectric material. POP is the dominant scattering mechanism for both *Cmcm* and *Amm2*, and PIE scattering is also considered in *Amm2* because of its lack of inversion symmetry. Similar to κ_{latt} , the electronic properties are also anisotropic (superior along the *a*- and

b-axes).

The predicted ZT of CsCu_2I_3 reaches 2.2 at 600 K along the *b*-axis ($n_e = 6 \times 10^{18} \text{ cm}^{-3}$), comparable to the ZT of state-of-the-art thermoelectric materials. The origin of high ZT is a combination of ultra-low κ_{latt} and high PF . η of 13.1 % is achievable when CsCu_2I_3 is used in a thermoelectric generator ($T_{\text{H}} = 600 \text{ K}$, $T_{\text{C}} = 200 \text{ K}$).

IV. METHODS

A. Density functional theory calculations

Calculations of the total energy, electronic band structure, and inputs for the AMSET package such as the dielectric, elastic, and piezoelectric constants were performed using density functional theory (DFT) within periodic boundary conditions through the Vienna *Ab Initio* Simulation Package (VASP) [50, 51]. Projector Augmented-Wave (PAW) [52, 53] method was employed to explicitly treat the valence state of Cs, Cu, and I atoms

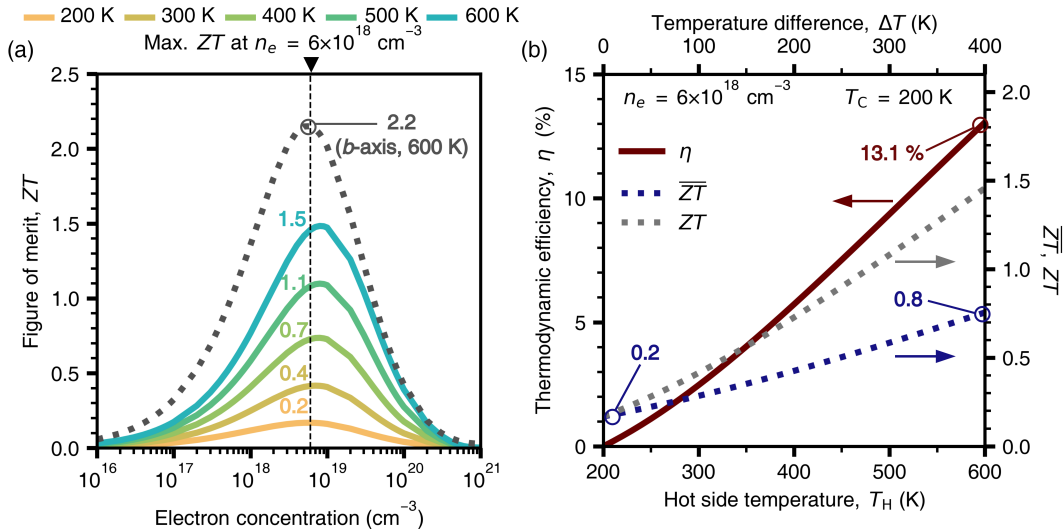


FIG. 10. (a) Calculated figure of merit (ZT) as a function of electron concentration and temperature. Isotropically averaged ZT are given by solid lines, and ZT along the b -axis (at 600 K) by the gray dotted line. (b) Thermodynamic efficiency (η , red), average ZT (\overline{ZT} , blue), and ZT (gray) as a function of the hot side temperature, T_H , of CsCu_2I_3 , $Amm2$ structure.

as 9 ($5s^25p^66s^1$), 17 ($2p^63d^{10}4s^1$), and 7 ($5s^25p^5$) electrons, respectively.

For structure optimization, the Perdew-Burke-Ernzerhof exchange-correlation (xc) functional revised for solids (PBEsol) [54] was used with a $6 \times 6 \times 8$ Γ -centered k -mesh, a plane-wave kinetic energy cutoff of 700 eV, and the convergence criteria set to 10^{-8} eV and 10^{-4} eV/Å for the total energy and atomic forces, respectively. The elastic and dielectric constant was calculated using the finite-displacement (FD) method and density functional perturbation theory (DFPT), respectively. The bulk modulus was calculated using the Phonopy [55] code by fitting the energy-volume to the third-order Birch-Murnaghan equation of state [56].

Calculations of the electronic band structure and electron transport were done using the hybrid DFT functional of Heyd, Scuseria, and Ernzerhof (HSE06) [57]. Compared to the structure optimization, a denser k -mesh of $12 \times 12 \times 16$ was used, while the kinetic energy cutoff was lowered to 400 eV. The hole and electron effective mass, m^* , was calculated using the sumo [58] code, which uses parabolic fitting by the following equation:

$$\frac{1}{m^*} = \frac{\partial^2 E(k)}{\partial k^2} \frac{1}{\hbar^2} \quad (5)$$

where $E(k)$ is the band energy as a function of the electron wavevector k , and \hbar is the reduced Planck's constant. The electronic band structure calculated above was used as the input.

B. Structure distortion

Harmonic level phonon calculations were performed using the Phonopy [55] code with VASP as the force calculator. The second-order interatomic force constants (IFCs) were computed using the supercell FD approach with a $3 \times 3 \times 3$ k -mesh, step size of 0.01 Å. A total of 11 displacements for $Cmcm$ and 22 displacements for $Amm2$ were calculated. A $2 \times 2 \times 3$ supercell of the 12-atom unit cell (144 atoms), was employed for both structures. The ModeMap [36] code was used to compute the displacement of the atoms, $u_{j,l}$ (j th atom in the l th unit cell), along an imaginary-mode eigenvector, $W_{\lambda,j}$ (λ is the phonon mode), at the Γ -point:

$$u_{j,l} = \frac{1}{\sqrt{n_a m_j}} \text{Re} \left[\sum_{\lambda} Q_{\lambda} W_{\lambda,j} e^{-iq \cdot r_{j,l}} \right] \quad (6)$$

where m_j is the atomic mass, n_a is the number of atoms in the supercell used to model the displacement, Q_{λ} is the distortion amplitude, q is the phonon wavevector, and $r_{j,l}$ is the atomic position. Post processing was also performed using the code to map the energy, $\Delta U(Q)$, as a function of Q_{λ} along the given $W_{\lambda,j}$ (c.f. Fig. 4). The ground-state structure, $Amm2$, was then obtained using the structure at the energy minimum.

C. Phonon and electron transport

κ_{latt} calculations were carried out using the Phono3py [59] code, solving the linearized Boltzmann transport equation (BTE) using the single-mode relaxation-time

approximation (RTA) (Eq. (2)). The third-order IFCs were calculated with a FD step size of 0.03 Å, and a total of 5568 displacements were considered in a 48-atom unit cell. A q -mesh of $12 \times 12 \times 16$ was employed to compute the lattice thermal conductivity. Graphical analysis of the modal properties were performed using the Phonopy-power-tool [42] code. Convergence tests for the lattice thermal conductivity over q -mesh, and distribution of force norms for the force sets can be found in Fig. S6.

Unlike the BoltzTraP [60] code, the AMSET [61] package uses DFT band structures to solve the BTE without the constant RTA. The characteristic scattering rate, τ_e , is calculated using the Matthiessen's rule:

$$\frac{1}{\tau_e} = \frac{1}{\tau_{\text{ADP}}} + \frac{1}{\tau_{\text{IMP}}} + \frac{1}{\tau_{\text{POP}}} + \frac{1}{\tau_{\text{PIE}}} \quad (7)$$

The mode dependent scattering rates, from state $|n\mathbf{k}\rangle$ to state $|m\mathbf{k} + \mathbf{q}\rangle$, is calculated using Fermi's golden rule:

$$\tilde{\tau}_{n\mathbf{k} \rightarrow m\mathbf{k} + \mathbf{q}}^{-1} = \frac{2\pi}{\hbar} |g_{nm}(\mathbf{k}, \mathbf{q})|^2 \delta(\varepsilon_{n\mathbf{k}} - \varepsilon_{m\mathbf{k} + \mathbf{q}}) \quad (8)$$

where ε is the electron energy, δ is the Dirac delta function and g is the coupling matrix element. The electron transport properties were computed by the generalized transport coefficients:

$$L_{\alpha\beta}^n = e^2 \int \sum_{\alpha\beta} (\varepsilon) (\varepsilon - \varepsilon_F)^n \left[-\frac{\partial f^0}{\partial \varepsilon} \right] d\varepsilon \quad (9)$$

where α and β denotes Cartesian coordinates, $\Sigma_{\alpha\beta}(\varepsilon)$ is the spectral conductivity, ε_F is the fermi level at a certain doping concentration and temperature, and f^0 is the Fermi-Dirac distribution. The properties are obtained as

$$\sigma_{\alpha\beta} = L_{\alpha\beta}^0 \quad (10)$$

$$S_{\alpha\beta} = \frac{1}{eT} \frac{L_{\alpha\beta}^1}{L_{\alpha\beta}^0} \quad (11)$$

$$\kappa_{\alpha\beta} = \frac{1}{e^2 T} \left[\frac{(L_{\alpha\beta}^1)^2}{L_{\alpha\beta}^0} - L_{\alpha\beta}^2 \right] \quad (12)$$

As mentioned above, the required material parameters such as the dielectric, elastic, and piezoelectric constants, phonon frequencies, and deformation potential were determined by DFT calculations (Table S1). As the valence bands are relatively flat, calculations were only conducted under n-type doping conditions, in the doping range from 10^{16} to 10^{21} , and the temperature range from 200 K to 600 K. The interpolation factor was set to 10 for all AMSET calculations. Convergence tests for the electron transport calculations over k -mesh and the interpolation factor can be found in Fig. S5.

ACKNOWLEDGMENTS

This work was supported by a National Research Foundation of Korea (NRF) grant funded by the Korean government (MSIT) (No. 2018R1C1B6008728). Via membership of the UK's HEC Materials Chemistry Consortium, which is funded by EPSRC (EP/L000202), this work used the ARCHER2 UK National Supercomputing Service (<http://www.archer2.ac.uk>).

The authors declare that they have no competing financial interests or personal relationships that could have influenced the work reported in this paper.

An online repository containing the basic bulk properties, force constant sets, and raw AMSET input/output files have been made available at <https://doi.org/10.1101/2021.03.11.437111>. [link will be added later].

J.W.P. performed the calculations and data analysis, and wrote the original draft under the supervision of Y.-K.J. and A.W. All authors contributed to discussing the results.

-
- [1] L. E. Bell, Stability of nonlinear modes, *Science* **321**, 1457 (2008).
- [2] A. Jain, Y. Shin, and K. A. Persson, Computational predictions of energy materials using density functional theory, *Nature Rev. Mater.* **1**, 1 (2016).
- [3] P. Gorai, V. Stevanović, and E. S. Toberer, Computationally guided discovery of thermoelectric materials, *Nature Rev. Mater.* **2**, 1 (2017).
- [4] K. B. Spooner, A. M. Ganose, W. W. Leung, J. Buckner, B. A. Williamson, R. G. Palgrave, and D. O. Scanlon, BaBi₂O₆: A promising n-type thermoelectric oxide with the PbSb₂O₆ crystal structure, *Chem. Mater.* **33**, 7441 (2021).
- [5] T. Deng, J. Recatala-Gomez, M. Ohnishi, D. V. M. Repaka, P. Kumar, A. Suwardi, A. Abutaha, I. Nandhakumar, K. Biswas, M. B. Sullivan, G. Wu, J. Shiomi, S.-W. Yang, and K. Hippalgaonkar, Electronic transport descriptors for the rapid screening of thermoelectric materials, *Mater. Horiz.* **8**, 2463 (2021).
- [6] S. Hao, V. P. Dravid, M. Kanatzidis, and C. Wolverton, Computational strategies for design and discovery of nanostructured thermoelectrics, *npj Comput. Mater.* **5**, 58 (2019).
- [7] R. D. M., *CRC handbook of thermoelectrics* (CRC press, Boca Raton, 2010).
- [8] A. Kojima, K. Teshima, Y. Shirai, and T. Miyasaka, Organometal Halide Perovskites as Visible-Light Sensitizers for Photovoltaic Cells, *J. Am. Chem. Soc.* **131**, 6050 (2009).
- [9] B. Lee, C. C. Stoumpos, N. Zhou, F. Hao, C. Malliakas,

- C.-Y. Yeh, T. J. Marks, M. G. Kanatzidis, and R. P. Chang, Air-stable molecular semiconducting iodosalts for solar cell applications: Cs_2SnI_6 as a hole conductor, *J. Am. Chem. Soc.* **136**, 15379 (2014).
- [10] Z.-K. Tan, R. S. Moghaddam, M. L. Lai, P. Docampo, R. Higler, F. Deschler, M. Price, A. Sadhanala, L. M. Pazos, D. Credgington, *et al.*, Bright light-emitting diodes based on organometal halide perovskite, *Nat. Nanotechnol.* **9**, 687 (2014).
- [11] T. Jun, K. Sim, S. Iimura, M. Sasase, H. Kamioka, J. Kim, and H. Hosono, Lead-Free Highly Efficient Blue-Emitting $\text{Cs}_3\text{Cu}_2\text{I}_5$ with 0D Electronic Structure, *Adv. Mater.* **30**, 1804547 (2018).
- [12] Z. Xiao, Y. Yuan, Y. Shao, Q. Wang, Q. Dong, C. Bi, P. Sharma, A. Gruverman, and J. Huang, Giant switchable photovoltaic effect in organometal trihalide perovskite devices, *Nat. Mater.* **14**, 193 (2015).
- [13] J.-M. Yang, Y.-K. Jung, J.-H. Lee, Y. C. Kim, S.-Y. Kim, S. Seo, D.-A. Park, J.-H. Kim, S.-Y. Jeong, I.-T. Han, *et al.*, Asymmetric carrier transport in flexible interface-type memristor enables artificial synapses with sub-femtojoule energy consumption, *Nanoscale Horiz.* **6**, 987 (2021).
- [14] A. Pisoni, J. Jacimovic, O. S. Barisic, M. Spina, R. Gaál, L. Forró, and E. Horváth, Ultra-low thermal conductivity in organic-inorganic hybrid perovskite $\text{CH}_3\text{NH}_3\text{PbI}_3$, *J. Phys. Chem. Lett.* **5**, 2488 (2014).
- [15] W. Lee, H. Li, A. B. Wong, D. Zhang, M. Lai, Y. Yu, Q. Kong, E. Lin, J. J. Urban, J. C. Grossman, *et al.*, Ultralow thermal conductivity in all-inorganic halide perovskites, *Proc. Natl. Acad. Sci. U. S. A.* **114**, 8693 (2017).
- [16] M. A. Haque, A. N. Gandhi, R. Mohanraman, Y. Wang, B. Davaasuren, A. H. Emwas, C. Combe, D. Baran, A. Rothenberger, U. Schwingenschlögl, H. N. Alshareef, S. Dong, and T. Wu, A 0D Lead-Free Hybrid Crystal with Ultralow Thermal Conductivity, *Adv. Funct. Mater.* **29**, 1809166 (2019).
- [17] W. Tang, T. Liu, and O. Fenwick, High thermoelectric performance based on CsSnI_3 thin films with improved stability, *J. Mater. Chem. A* **10**, 7020 (2020).
- [18] H. Xie, S. Hao, J. Bao, T. J. Slade, G. J. Snyder, C. Wolverton, and M. G. Kanatzidis, All-inorganic halide perovskites as potential thermoelectric materials: dynamic cation off-centering induces ultralow thermal conductivity, *J. Am. Chem. Soc.* **142**, 9553 (2020).
- [19] T. Liu, X. Zhao, J. Li, Z. Liu, F. Liscio, S. Milita, B. C. Schroeder, and O. Fenwick, Enhanced control of self-doping in halide perovskites for improved thermoelectric performance, *Nat. Commun.* **10**, 5750 (2019).
- [20] S. Yu, F. Qian, M. Hu, Z. Ge, J. Feng, and X. Chong, Enhanced thermoelectric performance in inorganic CsSnI_3 perovskite by doping with PbI_2 , *Mater. Lett.* **308**, 131127 (2022).
- [21] F. Qian, M. Hu, J. Gong, C. Ge, Y. Zhou, J. Guo, M. Chen, Z. Ge, N. P. Padture, Y. Zhou, and J. Feng, Enhanced thermoelectric performance in lead-free inorganic $\text{CsSn}_{1-x}\text{Ge}_x\text{I}_3$ perovskite semiconductors, *J. Phys. Chem. C* **124**, 11749 (2020).
- [22] T. Haeger, M. Wilmes, R. Heiderhoff, and T. Riedl, Simultaneous mapping of thermal conductivity, thermal diffusivity, and volumetric heat capacity of halide perovskite thin films: a novel nanoscopic thermal measurement technique, *J. Phys. Chem. Lett.* **10**, 3019 (2019).
- [23] G. A. Elbaz, W. L. Ong, E. A. Doud, P. Kim, D. W. Paley, X. Roy, and J. A. Malen, Phonon speed, not scattering, differentiates thermal transport in lead halide perovskites, *Nano Lett.* **17**, 5734 (2017).
- [24] T. Haeger, M. Ketterer, J. Bahr, N. Pourdavoud, M. Runkel, R. Heiderhoff, and T. Riedl, Thermal properties of CsPbCl_3 thin films across phase transitions, *J. Phys. Mater.* **3**, 024004 (2020).
- [25] A. Bhui, T. Ghosh, K. Pal, K. S. Rana, K. Kundu, A. Soni, and K. Biswas, Intrinsically low thermal conductivity in the n-type vacancy-ordered double perovskite Cs_2SnI_6 : octahedral rotation and anharmonic rattling, *Chem. Mater.* **34**, 3301 (2022).
- [26] Z. Zeng, C. Chen, C. Zhang, Q. Zhang, and Y. Chen, Critical phonon frequency renormalization and dual phonon coexistence in layered ruddlesden-popper inorganic perovskites, *Phys. Rev. B* **105**, 184303 (2022).
- [27] P. Acharyya, T. Ghosh, K. Pal, K. Kundu, K. S. Rana, J. Pandey, U. V. Soni, A. Waghmare, and K. Biswas, Intrinsically ultralow thermal conductivity in Ruddlesden-Popper 2D perovskite $\text{Cs}_2\text{PbI}_2\text{Cl}_2$: localized anharmonic vibrations and dynamic octahedral distortions, *J. Am. Chem. Soc.* **142**, 15595 (2020).
- [28] Y.-K. Jung, I. T. Han, Y. C. Kim, and A. Walsh, Prediction of high thermoelectric performance in the low-dimensional metal halide $\text{Cs}_3\text{Cu}_2\text{I}_5$, *npj Comput. Mater.* **7**, 51 (2021).
- [29] L.-D. Zhao, S.-H. Lo, Y. Zhang, H. Sun, G. Tan, C. Uher, C. Wolverton, V. P. Dravid, and M. G. Kanatzidis, Ultralow thermal conductivity and high thermoelectric figure of merit in SnSe crystals, *Nature* **508**, 373 (2014).
- [30] I. Pallikara, P. Kayastha, J. M. Skelton, and L. D. Whalley, The physical significance of imaginary phonon modes in crystals, *Electron. Struct.* **4**, 033002 (2022).
- [31] N. Jouini, L. Guen, and M. Tournoux, Structure cristalline de CsCu_2I_3 , *Rev. Chim. Mineral* **17**, 486–(1980).
- [32] T. Jun, T. Handa, K. Sim, S. Iimura, M. Sasase, J. Kim, Y. Kanemitsu, and H. Hosono, One-step solution synthesis of white-light-emitting films via dimensionality control of the Cs–Cu–I system, *APL Mater.* **7**, 111113 (2019).
- [33] R. Roccanova, A. Yangui, G. Seo, T. D. Creason, Y. Wu, D. Y. Kim, M. H. Du, and B. Saparov, Bright luminescence from nontoxic CsCu_2X_3 ($X = \text{Cl}, \text{Br}, \text{I}$), *ACS Materials Lett.* **1**, 459 (2019).
- [34] A. Jain, S. P. Ong, G. Hautier, W. Chen, W. D. Richards, S. Dacek, S. Cholia, D. Gunter, D. Skinner, G. Ceder, and K. A. Persson, Commentary: The Materials Project: A materials genome approach to accelerating materials innovation, *APL Materials* , 011022 (2013).
- [35] J. Sun and C. A. Ullrich, Optical properties of CsCu_2X_3 ($X = \text{Cl}, \text{Br}, \text{and I}$): A comparative study between hybrid time-dependent density-functional theory and the Bethe-Salpeter equation, *Phys. Rev. Materials* **4**, 095402 (2020).
- [36] J. M. Skelton, L. A. Burton, S. C. Parker, A. Walsh, C. E. Kim, A. Soon, J. Buckeridge, A. A. Sokol, C. R. Catlow, A. Togo, and I. Tanaka, Anharmonicity in the high-temperature Cmcm phase of SnSe : soft modes and three-phonon interactions, *Phys. Rev. Lett.* , 075502 (2016).
- [37] S. Cheng, A. Beitlerova, R. Kucerkova, E. Mihokova, M. Nikl, Z. Zhou, G. Ren, and Y. Wu, Non-hygroscopic, self-absorption free, and efficient 1D CsCu_2I_3 perovskite single crystal for radiation detection, *ACS Appl. Mater. Interfaces* **13**, 12198 (2021).

- [38] F. Serrano-Sánchez, M. Gharsallah, N. M. Nemes, F. J. Mompean, J. L. Martínez, and J. A. Alonso, Record Seebeck coefficient and extremely low thermal conductivity in nanostructured SnSe, *Appl. Phys. Lett.* , 083902 (2015).
- [39] P. Ying, X. Li, Y. Wang, J. Yang, C. Fu, W. Zhang, X. Zhao, and T. Zhu, Hierarchical Chemical bonds contributing to the intrinsically low thermal conductivity in α -MgAgSb thermoelectric materials, *Adv. Funct. Mater.* , 1604145 (2017).
- [40] W. Rahim, J. M. Skelton, and D. O. Scanlon, $\text{Ca}_4\text{Sb}_2\text{O}$ and $\text{Ca}_4\text{Bi}_2\text{O}$: two promising mixed-anion thermoelectrics, *J. Mater. Chem. A* , 20417 (2021).
- [41] L. D. Zhao, C. Chang, G. Tan, and M. G. Kanatzidis, SnSe: a remarkable new thermoelectric material, *Energy Environ. Sci.* , 3044 (2016).
- [42] Software repository, <https://github.com/skelton-group/Phono3py-Power-Tools> ((accessed March 20, 2022)).
- [43] L. D. Whalley, J. M. Skelton, J. M. Frost, and A. Walsh, Phonon anharmonicity, lifetimes, and thermal transport in $\text{ch}_3\text{nh}_3\text{pb}_i_3$ from many-body perturbation theory, *Phys. Rev. B* **94**, 220301 (2016).
- [44] Y.-K. Jung, J. Calbo, J.-S. Park, L. D. Whalley, S. Kim, and A. Walsh, Intrinsic doping limit and defect-assisted luminescence in Cs_4PbBr_6 , *Journal of Materials Chemistry A* **7**, 20254 (2019).
- [45] R. Lin, Q. Guo, Q. Zhu, Y. Zhu, W. Zheng, and F. Huang, All-Inorganic CsCu_2I_3 Single Crystal with High-PLQY ($\approx 15.7\%$) Intrinsic White-Light Emission via Strongly Localized 1D Excitonic Recombination, *Adv. Mater.* , 1905079 (2019).
- [46] J. Ma, Y. Chen, and W. Li, Intrinsic phonon-limited charge carrier mobilities in thermoelectric SnSe, *Phys. Rev. B* **97**, 205207 (2018).
- [47] J. Wei, L. Yang, Z. Ma, P. Song, M. Zhang, J. Ma, F. Yang, and X. Wang, Review of current high-ZT thermoelectric materials, *J. Mater. Sci.* , 12642 (2020).
- [48] E. Amerling, H. Lu, B. W. Larson, A. E. Maughan, A. Phillips, E. Lafalce, L. Whittaker-Brooks, J. J. Berry, M. C. Beard, Z. V. Vardeny, and B. J. L., A multi-dimensional perspective on electronic doping in metal halide perovskites, *ACS Energy Lett.* , 1104 (2021).
- [49] R. Fan, S. Fang, S. Liang, Z. Liang, and H. Zhong, Controllable one-step doping synthesis for the white-light emission of cesium copper iodide perovskites, *Photon. Res.* , 694 (2021).
- [50] G. Kresse and J. Furthmüller, Efficient iterative schemes for *ab initio* total-energy calculations using a plane-wave basis set, *Phys. Rev. B* **54**, 11169 (1996).
- [51] G. Kresse and J. Furthmüller, Efficiency of *ab-initio* total energy calculations for metals and semiconductors using a plane-wave basis set, *Comput. Mater. Sci.* **6**, 15 (1996).
- [52] G. Kresse and D. Joubert, From ultrasoft pseudopotentials to the projector augmented-wave method, *Phys. Rev. B* **59**, 1758 (1999).
- [53] P. E. Blöchl, Projector augmented-wave method, *Phys. Rev. B* **50**, 17953 (1994).
- [54] J. P. Perdew, A. Ruzsinszky, G. I. Csonka, O. A. Vydrov, G. E. Scuseria, L. A. Constantin, X. Zhou, and K. Burke, Restoring the density-gradient expansion for exchange in solids and surfaces, *Phys. Rev. Lett.* **100**, 136406 (2008).
- [55] A. Togo and I. Tanaka, First principles phonon calculations in materials science, *Scr. Mater.* **108**, 1 (2015).
- [56] F. Birch, Finite elastic strain of cubic crystals, *Phys. Rev.* **71**, 809 (1947).
- [57] J. Heyd, G. E. Scuseria, and M. Ernzerhof, Hybrid functionals based on a screened Coulomb potential, *J. Chem. Phys.* **118**, 8207 (2003).
- [58] A. M. Ganose, A. J. Jackson, and D. O. Scanlon, Command-line tools for plotting and analysis of periodic *ab initio* calculations, *J. Open Source Softw.* **3**, 717 (2018).
- [59] A. Togo, L. Chaput, and I. Tanaka, Distributions of phonon lifetimes in brillouin zones, *Phys. Rev. B* **91**, 094306 (2015).
- [60] G. K. Madsen and D. J. Singh, BoltzTraP. A code for calculating band-structure dependent quantities, *Comput. Phys. Commun.* , 67 (2006).
- [61] A. M. Ganose, J. Park, A. Faghaninia, R. Woodsrobinson, K. A. Persson, and A. Jain, Efficient calculation of carrier scattering rates from first principles, *Nat. Commun.* , 2222 (2021).